Thermal-wave resonator cavity

Jun Shen and Andreas Mandelis
Photothermal and Optoelectronic Diagnostics Laboratory, Center for Hydrogen and Electrochemical Studies (CHES), Department of Mechanical Engineering, University of Toronto, Toronto M5S 1A4, Canada

(Received 8 November 1994; accepted for publication 9 June 1995)

A thermal-wave resonant cavity was constructed using a thin aluminum foil wall as the intensity-modulated-laser-beam induced oscillator source opposite a pyroelectric polyvilidene fluoride wall acting as a signal transducer and cavity standing-wave-equivalent generator. It was shown that scanning the frequency of oscillation produces the fundamental and higher overtone resonant extrema albeit with increasingly attenuated amplitude—a characteristic of thermal-wave behavior. Experimentally, scanning the cavity length produced a sharp lock-in in-phase resonance with simple linewidth dependencies on oscillation (chopping) frequency and intracavity gas thermal diffusivity. The thermal diffusivity of air at 294 K was measured with three significant figure accuracy: 0.211 ± 0.004 cm^2/s. The novel resonator can be used as a high-resolution thermophysical property sensor of gaseous ambients. © *1995 American Institute of Physics.*

I. INTRODUCTION

Traditionally thermal-wave generation and detection in condensed phases involves the scanning of the modulation frequency of the source medium intensity, usually a chopped laser beam. Amplitude and phase spectra are thus obtained, which have been conveniently and successfully modeled (using propagating wave language) as representing the superposition of forward- and backward-propagating thermal waves in an excited sample of finite thickness. As a result, the behavior of the detected frequency scan can be explained by summing up the entire wave train which forms a spatial interference pattern.[1] The attribution of propagating wave-field properties to diffusive, spatially heavily damped temperature oscillations in a medium of finite thickness, either in the form of the spatial superposition of counterpropagating thermal waves,[1] or by use of well-known sourcing techniques involving energy reflections at material boundaries (e.g., the method of images)[2,3] is, in fact, invoked only for mathematical convenience and has been experimentally[4] justified through its well-documented agreement with experimental amplitude and phase results obtained by a number of investigators.[5] Even though the foregoing approaches *do yield* excellent theoretical fittings of data obtained under a great variety of conditions and geometries, and they predict reliable values of thermophysical properties in very good agreement with those obtained independently by nonphotothermal techniques, nevertheless it must be emphasized that the *interpretation* of the fitted data in terms of standing thermal-wave fields, or as a result of thermal-energy interreflections from geometric boundaries of a given experimental configuration, should be made with the utmost caution. Unlike conventional propagating wave fields, and despite the prevailing descriptions of the propagation of thermal waves in the literature, diffusive temperature-wave behavior cannot sustain reflections at the boundaries where the thermophysical properties change abruptly, because conduction heat transfer is unidirectional and only activated by existing temperature gradients which generate net heat fluxes in the appropriate directions in a material according to the continuity equation[6]

$$-k\nabla T(\mathbf{r},t)=\mathbf{F}(\mathbf{r},t), \tag{1}$$

where $\mathbf{F}$ is the thermal flux, T is the temperature, and k is the thermal conductivity of the material. The existence, however, of a discontinuity in the thermal properties (specifically the thermal effusivity) across a material interface does cause the *rate* of forward propagation to change at that boundary.

If the boundary delineates passage to a region with poorer thermal effusivity, such as is the case with the air–polymer interface considered in this work, then the forward thermal-wave flux decreases. This effect can be described mathematically by the addition of a backward propagating thermal-wave source in the spatial region immediately after the boundary, or, equivalently, by the introduction of a "reflected thermal ray" into the region before the boundary. This, of course, cannot occur physically in view of Eq. (1), since a counterpropagating thermal-energy field would be in conflict with the pre-existing forward direction of the temperature gradient. Nevertheless, in the presence of the thermal obstruction at the boundary, either of these mathematical constructs results in an excess amount of thermal power localized in the before-the-boundary spatial region, *equal to that which would have been introduced if an image source or a thermal-wave reflection were physically possible.* In the case of the mathematical representation by "reflected" thermal waves, the counterpropagating nature of these waves can be further exploited to predict the presence of "standing thermal waves," as first done by Bennett and Patty.[1] It should be clear from the foregoing that no such standing waves are possible. Physically, however, the confined excess thermal-wave power in the before-the-boundary region contributes to forming locally different phase relationships from that which would exist if the boundary obstruction were absent. The accumulation of modulated thermal power in this region forms a node and antinode pattern of the thermal-wave field which can be accurately described mathematically by a standing-wave pattern created by infinite inter-reflections of the thermal wave fronts across the front and backboundaries of the confined spatial region under consideration.

Conversely, if the boundary accosted by the forwardly

propagating thermal wave marks the passage to a region with better thermophysical properties (i.e., thermal effusivity) than the confinement region, the thermal-wave flux increases in the direction of the temperature gradient. The presence of the heat sink can be described mathematically by the subtraction of a thermal-wave source or a negative reflection term. The net result of these mathematical constructs is an extracted amount of thermal power from the before-the-boundary spatial region, *equal to that which would have been missing if an image heat sink or a negative thermal-wave reflection were physically possible*. The counterpropagating nature of the negative reflections can also be shown to result mathematically in a standing-thermal-wave pattern of nodes and antinodes in the confinement region. This pattern exhibits lower antinode intensity than the one stemming from the positive reflection superpositions in the foregoing case.

In this work, exploiting further the mathematical analog of confined thermal-wave propagation to standing thermal waves in gaseous ambients, and in the context of recent instrumental developments,[7] we report the first experimental observation of a spatial pattern which is consistent with a cavity resonance due to standing waves when the cavity length is properly tuned to an antinode position in the medium of propagation. This type of variable-length cavity has been called a *thermal-wave resonator cavity* by analogy to properly traveling (i.e., nondiffusive) wave-field resonators.

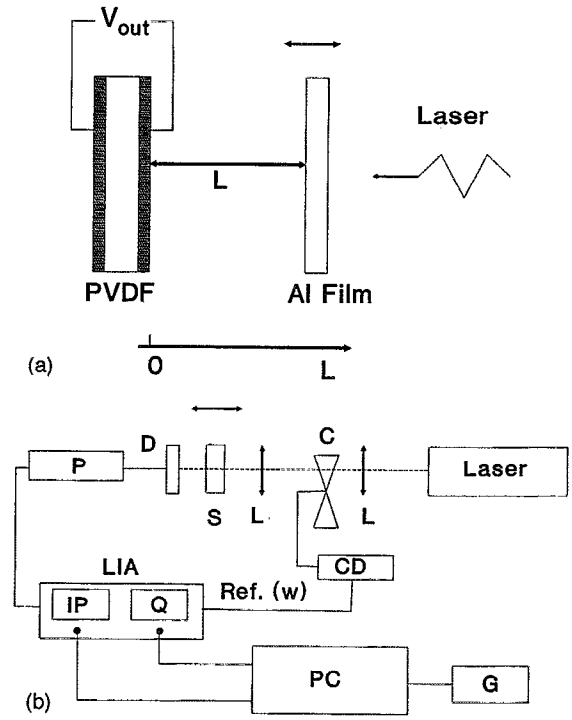

FIG. 1. (a) Schematic of thermal-wave resonator cavity. (b) Block diagram of the experimental system used for the excitation and observation of the thermal-wave resonances L: lens; C: mechanical chopper, S: aluminum wall of thermal-wave cavity; D: PVDF cavity wall and detector; P: preamplifier; LIA: lock-in amplifier; C D: chopper driver; PC: Computer; G: plotter.

II. INSTRUMENTATION AND CAVITY THEORY

A. Thermal-wave resonator cavity construction

The ability to scan laser-beam intensity modulation frequencies has been the most powerful control parameter of the experimenter in the dynamic thermal-wave probing of matter to date. The recent development of a photopyroelectric (PPE) detector with a variable sample-to-source distance,[7] however, has introduced the variability of the thermal-wave cavity length at a single modulation frequency as another, equally powerful, control parameter. This scheme exhibits a higher signal-to-noise ratio (SNR) than frequency-scanned schemes, because the instrumental transfer function remains constant during the experiment, following its optimization at a single cavity length, thus fixing the noise bandwidth throughout the scan.[8] Furthermore, given the proven adequacy of the mathematical description of the confined thermal wave between two interfacial boundaries in terms of a spatially resolved standing-wave pattern,[1,6] one may expect that the ability to vary the sample-to-detector distance can take advantage of the well-known characteristics of this pattern and tune it to a resonance condition, in a manner familiar from the resonances observed in optical or acoustical cavities, but with a heavily damped spatial profile, somewhat similar to a damped harmonic oscillator upon interchange between the time and space variables. The situation, of course, is very different from that prevailing in optical or acoustical resonators, since there one deals with freely traveling and counterpropagating waves.

A major effort in this work was the construction of the first thermal-wave resonator cavity with variable length, and the study of the nature of the cavity resonance condition. A block diagram of the cavity geometry is shown in Fig. 1(a). One cavity wall was simply made by mounting a 15-μm-thick aluminum foil on a circular ring so as to form a stretched, flat surface of $\sim$1 cm diam. The other wall was the surface of a pyroelectric polyvinylidene fluoride (PVDF) thin film circular sensor, 52 μm thick and 0.8 cm in diameter, enclosed in a modified Inficon™ housing which acts simultaneously as a mechanical support and pyroelectric thermal-wave signal detector and transducer. The PVDF-film sensor is a pyroelectric polymer energy-conversion transducer,[9] which operates in either the open-circuit-voltage or the short-circuit-current signal generation mode. In the former (lower-noise) mode, the sensor generates an ac voltage across its electrode surfaces proportional to a temperature oscillation (thermal wave) on the PVDF surface. The PVDF side of the parallel-wall cavity was mounted on a micrometer stage, which allowed the cavity length to vary as desired with a 10 μm step resolution. The experimental setup is shown in block form in Fig. 1(b). The aluminum foil surface exterior to the cavity was sooted lightly in order to enhance optical absorption and thermal-wave signal generation from a mechanically chopped 10 mW He–Ne laser incident normal to the surface, while remaining entirely thermally thin in the frequency range 1–20 Hz. Indeed, from the average reported value of thermal diffusivity of aluminum (α_{Al}=0.85 cm^2/s),[10]

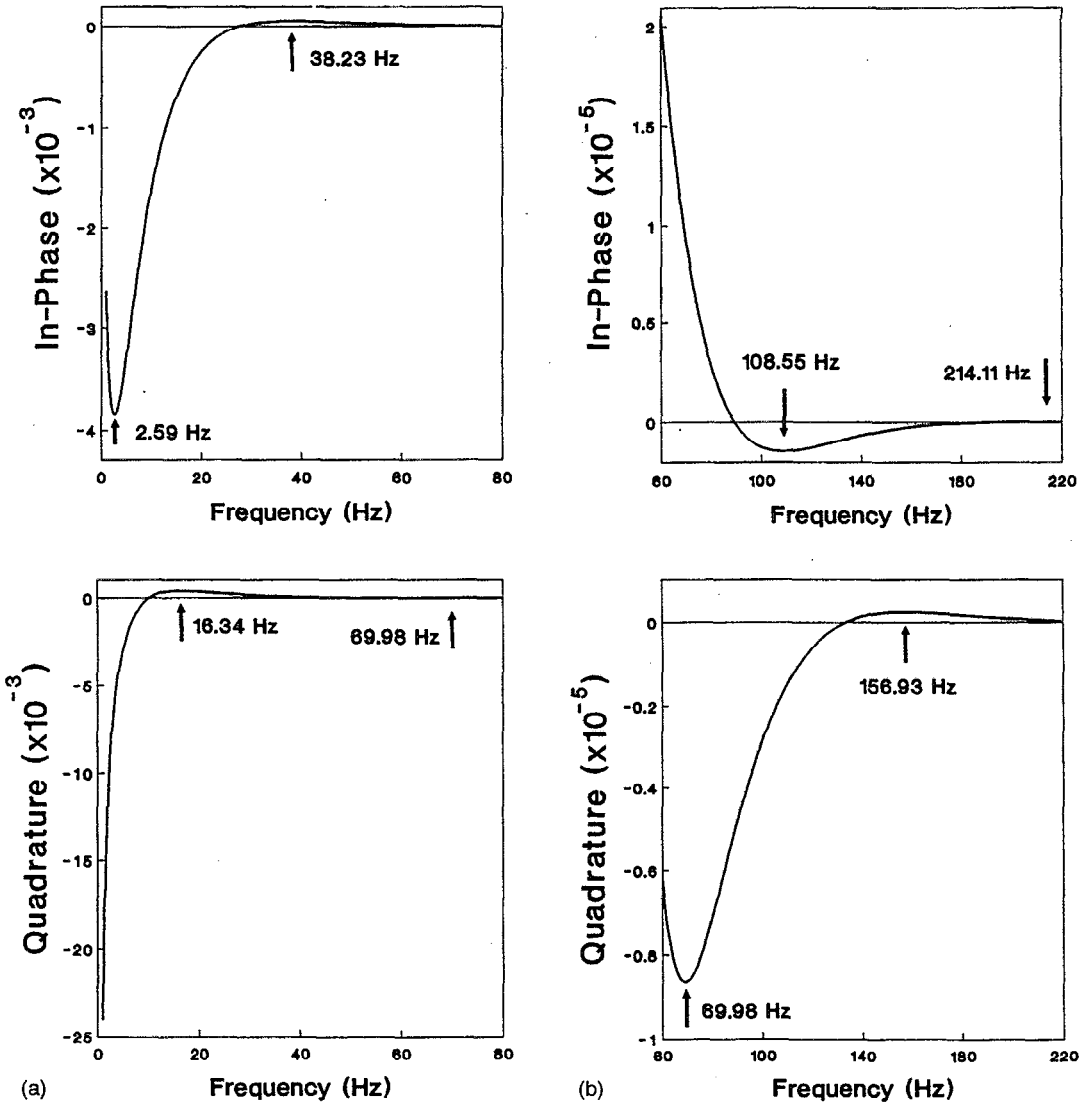

FIG. 2. Theoretical lock-in in-phase (IP) and quadrature (Q) line shapes of thermal-wave resonances as functions of laser-beam modulation frequency in a cavity with length $L=0.2$ cm, aluminum and PVDF walls, and gas (air) thermal diffusivity $\alpha_g=0.22$ cm^2/s. Frequency scan: (a) 0–80 Hz; (b) 60–220 Hz.

the shortest thermal diffusion length in this frequency range, is given by[6]

$$\mu(f)=\sqrt{\frac{\alpha_{\mathrm{Al}}}{\pi f}}. \tag{2}$$

In aluminum this can be calculated to be 1.16 mm $\gg$15 μm, i.e., the foil was totally thermally thin. This requirement is necessary in order to preserve the phase of the thermal wave across the foil thickness, thus maximizing the lock-in in-phase resonance peak without rotating the cavity phasor [tan-

TABLE I.

n	$f_R^{(n)}$ (Hz)	$\Delta f_R^{(n)}$ (Hz)	$\lambda_R^{(n)}$ (cm)	$Q_n^{(\mathrm{IP})}$	$Q_n^{(Q)}$	$2L/\lambda_R^{(n)}$
In-phase channel						
1	2.59	8.08	1.04	0.32		0.38
2	38.23	25.52	0.27	1.50		1.47
3	108.55	43.53	0.16	2.49		2.48
4	214.11	61.50	0.11	3.48		3.49
Quadrature channel						
1	16.34	16.37	0.41		0.30	0.96
2	69.99	34.59	0.20		1.30	1.98
3	156.93	52.52	0.13		2.93	2.99
4	280.09	70.48	0.10		5.22	3.99

tamount to mixing the lock-in amplifier-in-phase (IP) and quadrature (Q) components]. The rest of the instrumental geometry in Fig. 1(b) is standard for thermal-wave measurements.

The dependence of the PPE thermal-wave signal on the cavity length L is[7]

$$V(L,\alpha_g,\omega)=\text{const}\times\frac{\exp(-\sigma_g L)}{1-\gamma_{gs}\gamma_{gp}\exp(-2\sigma_g L)}, \quad (3)$$

where α_g is the complex thermal-wave diffusion coefficient

$$\sigma_g=(1+i)\sqrt{\omega/2\alpha_g} \quad (4)$$

and γ_{jk} are thermal coefficients at the $(j-k)$ interface (g: gas; s: solid wall (aluminum foil); and p: PVDF wall), defined as

$$\gamma_{jk}\equiv\frac{(1-b_{jk})}{(1+b_{jk})}; \quad b_{jk}\equiv\frac{\alpha_j\sqrt{K_k}}{\alpha_k\sqrt{K_j}}. \quad (5)$$

Here b_{jk} are the thermal coupling coefficients at the interface between media (j) and (k); K denotes thermal conductivity, and ω is the angular modulation frequency of the thermal wave. The only assumptions underlying Eq. (3) are (a) the complete opacity of the surface on which the laser radiation impinges (validated in this case by the sooted aluminum foil), and (b) the one dimensionality of the thermal-wave response of the cavity, valid when the laser beam diameter is large compared to the thermal diffusion length μ_g in the cavity (~0.6 and ~0.06 cm, respectively, in the present setup).

B. Frequency resonances and the quality factor (Q) of the cavity

Standing thermal-wave mode patterns are formed in the cavity of length L, loosely similar to the acoustical open-ended "organ-pipe" resonances,[11] but unlike the optical-cavity (Fabry–Perot) counterparts.[12] This is so owing to the similarities of the boundary conditions between the acoustical open-ended pipe and the thermal-wave cavity: They both exhibit an antinode at one boundary (end) plane. For the thermal-wave cavity this end plane is the thin metal-foil front wall on which the incident laser irradiation is converted into a temperature oscillation. For the acoustic cavity there may be one or two antinodes at the end planes, depending on whether one or both pipe ends are open. There is no *a priori* constraint (nodal or antinodal boundary condition) at the other end plane of the thermal-wave cavity. In principle, an antinode exists there if the backwall is a perfect thermal insulator ($b_{gp}=\infty$; $\gamma_{gp}=-1$). A node exists there if the backwall is a perfect thermal conductor ($b_{gp}=0$; $\gamma_{gp}=1$). For all physical wall materials the actual value of γ_{gp} is in the range $[-1,+1]$ and determines the fraction of thermal-wave power "reflected" to form standing waves. On the other hand, the optical Fabry–Perot resonator forms nodal patterns at both cavity end planes. Therefore, it is not an analog to the thermal-wave resonator.

Under standing-wave conditions, significant thermal-wave-field enhancement may be expected to occur at resonances of the cavity. Figure 2 shows theoretical frequency

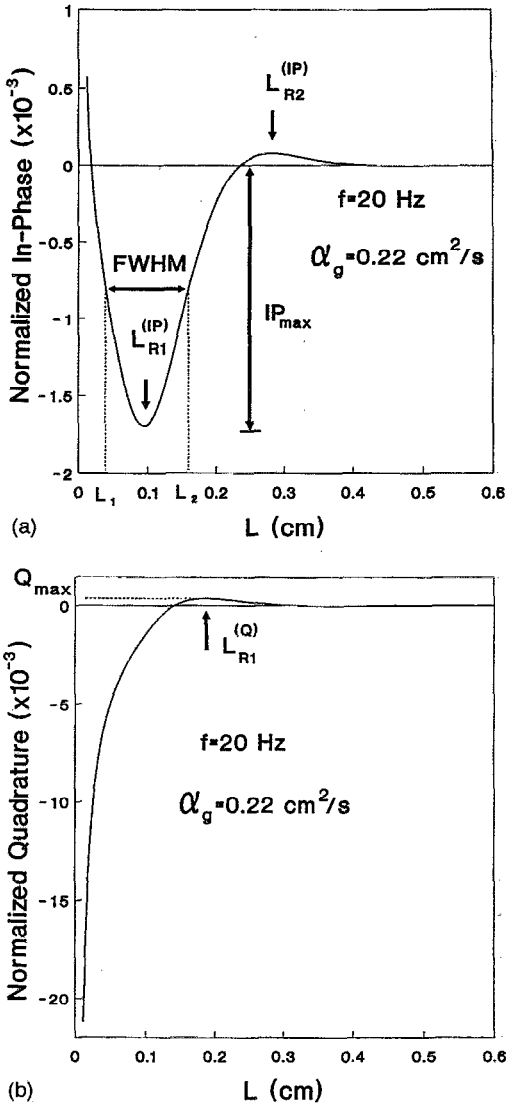

FIG. 3. (a) Theoretical lock-in IP-channel lineshape of thermal-wave fundamental and first overtone resonances as a function of length in a cavity with $f=20$ Hz and gas thermal diffusivity $\alpha_g=0.22$ cm^2/s. The linewidth (FWHM) end points L_1 and L_2 are also shown; (b) The Q-channel fundamental resonance peak.

scans of the cavity of Fig. 1(a) with $L=0.2$ cm, aluminum wall thickness $l=15$ μm, and air as the gaseous medium confined between the walls. Calculations of the IP- and Q-signal channels of the lock-in amplifier were made, using aluminum, copper, or brass walls with the following parameters: $\alpha_{Al}=0.98$ cm^2/s,[13] $K_{Al}=2.37$ W/cm K,[13] $\alpha_{Cu}=1.12$ cm^2/s,[14] $K_{Cu}=3.86$ W/cm K,[14] $\alpha_{brass}=0.34$ cm^2/s,[14] $K_{brass}=1.11$ W/cm K,[14] $\alpha_{air}=0.22$ cm^2/s,[13] $K_{air}=2.62\times10^{-4}$ W/cm K,[13] $\alpha_{PVDF}=5.4\times10^{-4}$ cm^2/s,[15] $K_{PVDF}=1.3\times10^{-3}$ W/cm K.[15] In Fig. 2(a) the fundamental resonance antinode is shown for a cavity wall made of aluminum foil. It occurs at very low frequencies (2.59 Hz for the IP oscillation and 16.34 Hz for the Q oscillation). The IP-component exhibits a strong and narrow minimum, whereas the Q component gives a much weaker and broader maximum. These extrema are further followed by higher-frequency antinodes at 38.23 Hz (IP maximum) at 69.98 Hz (Q minimum) on Fig. 2(a). In

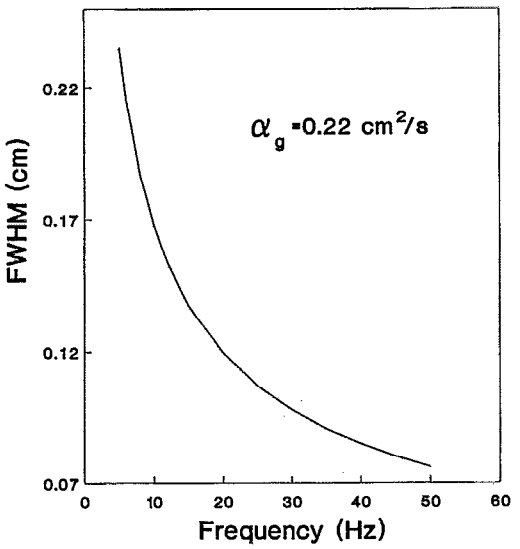

FIG. 4. Dependence of the fundamental IP resonant linewidth (L_2-L_1) on chopping frequency with air as intracavity gas; $L=0.2$ cm.

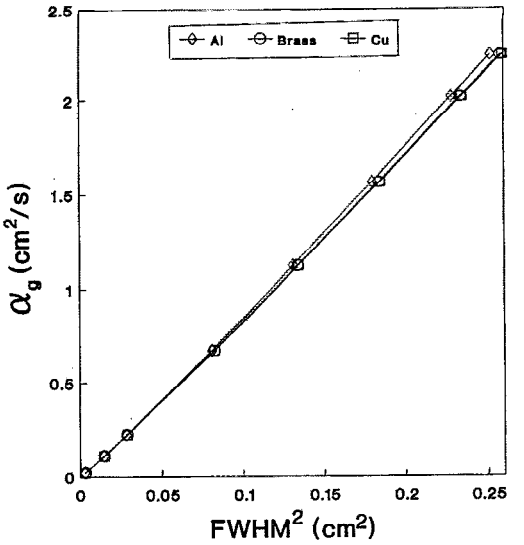

FIG. 5. Dependence of the fundamental IP resonant linewidth on intracavity gas thermal diffusivity for three wall materials at $f=10$ Hz and (assumed) wall thickness 15 μm.

order to enhance the visibility of the strongly attenuated overtones, the ordinate of Fig. 2(b) was amplified by $\times 10$ and the frequency range was gated to exclude the strong, low-frequency resonances. In the range 60–220 Hz, the Q channel exhibits a relatively strong and narrow minimum, followed by a broad maximum; the IP channel exhibits only weak and broad antinodes, Table I shows the frequencies of the four lowest IP- and Q-channel thermal-wave resonances in the cavity, $f_R^{(n)}$, the cavity linewidths, $\Delta f_R^{(n)}$, (full widths at half-maxima, FWHM) corresponding to these resonances, and the thermal wavelengths corresponding to the resonant frequencies given by

$$\lambda_R^{(n)}=2\sqrt{\frac{\pi\alpha_g}{f_R^{(n)}}}. \tag{6}$$

The linewidths shown in Table I were calculated with reference to the zero signal baselines. In analogy to traveling-wave fields, column 4 of Table I shows the value obtained for the cavity quality factor (Q factor) for each of the resonance peaks, defined as[11]

$$Q_n\equiv\frac{f_R^{(n)}}{\Delta f_R^{(n)}} \tag{17}$$

for either IP- or Q-channel resonance. It can be seen that the Q_n factors characterizing thermal-wave resonator cavities increase with increasing overtone frequency, thus offering improved peak resolution at higher frequencies. Nevertheless, they are extremely low in comparison with, for instance, optical Fabry–Perot resonant cavities which exhibit Q's greater than 10^8. These results are consistent with the extremely lossy (diffusive) nature of thermal-wave cavities. Finally, Table I shows the values of the quantity $2L/\lambda_R^{(n)}$ in column 5. There is excellent correlational "quantization" in the Q channel to the integer (n), which improves rapidly with increasing n (4% difference for $n=1$; 0.25% difference for $n=4$). The foregoing correlation can thus be written to a very good approximation in the form

$$L\approx n\,\frac{\lambda_R^{(n)}}{2};\quad n=1,2,3,4,\ldots\,. \tag{8}$$

which is the well-known antinodal condition for standing waves in an open-ended resonator, such as an uncapped pipe organ[11] as discussed earlier on. Therefore, in view of Eq. (8), the $n>1$ overtones of the thermal-wave cavity can be increasingly considered as "harmonics" of the fundamental cavity resonance frequency $f_R^{(1)}$. It is interesting to note from column 5 of Table I, that the IP-channel also obeys a half-integer quantization rule of the form

$$L\approx(n-\tfrac{1}{2})\,\frac{\lambda_R^{(n)}}{2};\quad n=1,2,3,4,\ldots, \tag{9}$$

which is the same as the antinodal condition for standing waves in a pipe resonator with the far end capped.[11] The departure of the fundamental from the ideal theoretical value ($n=1$) is the result of the shifting of the resonance peak to a lower value in Fig. 2(a) due to the exponential weighing factor in Eq. (3) which decreases steeply in this region and skews the position of the peak frequency toward the low end. This peak shift is more pronounced in the IP channel than in the Q channel, because the cos function in the real part of the numerator of Eq. (3) has a maximum at 0 Hz (i.e., at dc) where the exponential decay rate is steepest and greatly affects the position of the nearest maximum of the product function comprising the real part of the numerator. On the other hand, the sin function in the imaginary part of the numerator of Eq. (3) peaks at higher frequencies, where the decay of the exponential envelope is gentler, so the product function peaks much closer to the actual peak of the sin component, in a manner quite similar to the position of the antinode in open-ended cavities with standing longitudinal-wave patterns. It is for these reasons that the IP-channel resonance condition for the fundamental is in much poorer agreement with the ideal theoretical expression for $n=1$, Eq. (9), than is the Q-channel fundamental resonance with Eq. (8).

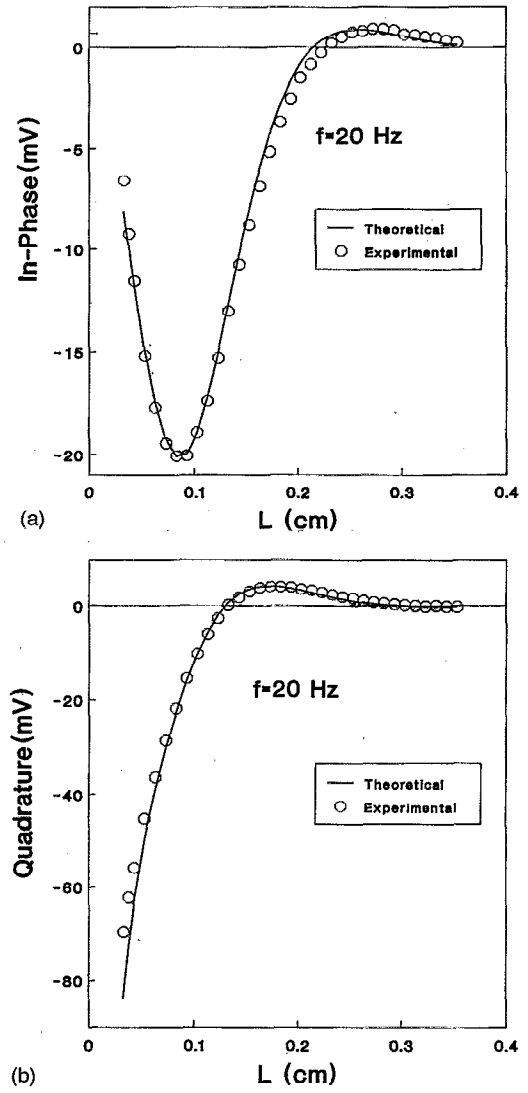

FIG. 6. Experimental and theoretical lineshapes obtained with $f=20$ Hz, and wall (aluminum foil) thickness 15 μm. (a) IP-channel data scan; and (b) Q-channel data scan. The best theoretical fit of Eq. (3) to both data curves yielded $\alpha_{air}=0.211\pm0.004$ cm^2/s at $T=294$ K.

Nevertheless, the IP-channel overtone resonance agreement with Eq. (9) improves very rapidly with increasing n (24% difference for $n=1$; 0.29% difference for $n=4$).

C. Cavity-length resonances

The condition for the length of a traveling-wave resonance-forming cavity[12] is that the phase of the thermal wave should return to its original value (plus an integral multiple of 2π) after one round trip in the cavity. It is easy to show from Eq. (3) that for thermal waves the Q-channel resonance condition is reduced to the familiar requirement that the cavity length must be equal to an integral number n of half-wavelengths as described by Eq. (8). Owing to the exponentially damped nature of thermal waves in space, in practice only the $n=1$ condition matters, for which

$$L_R^{(Q)}=\tfrac{1}{2}\lambda_{tw}; \quad \lambda_{tw}\equiv\lambda_R^{(1)}=2\sqrt{\pi\alpha_g/f}. \tag{10}$$

Here $f=\omega/2\pi$ and λ_{tw} corresponds to the geometry of Fig. 1(a) with the length L tuned so as to produce the resonance condition, Eq. (10). The resonant L appears with the subscript "R." Similarly, the IP-channel resonance condition is reduced to the requirement that the cavity length must be an integral number of quarter-wavelengths as described by Eq. (9). Here, again, only the $n=1$ condition matters in practice, for which

$$L_R^{(IP)}=\tfrac{1}{4}\lambda_{tw}.$$

Figure 3(a) shows the theoretical IP resonance lineshape for a cavity of variable L, with the peak (trough) occurring at $L=\frac{1}{4}\lambda_{tw}$, which renders the cavity a thermal-wave resonator. A secondary peak appears when L is changed to a larger value corresponding to the second overtone of the cavity: $L=3\lambda_{tw}/4$, Eq. (9). The Q-channel line shape in Fig. 3(b) is much broader than the IP counterpart. Here the (weak) peak occurs at the fundamental resonance condition $L=\frac{1}{2}\lambda_{tw}$, as expected from Eq. (8). *In conclusion, thermal-wave cavity resonances are most likely to be observed and utilized for accurate thermophysical measurements in gaseous ambients by use of the IP channel of the lock-in amplifier (photo)pyroelectric signal.*

III. EXPERIMENT AND RESULTS

The positional measurement of the peak in Fig. 3(a) depends on the accurate knowledge of the *absolute value* of L, which is not an easy task, given the extreme sensitivity of the thermal-wave decay envelope on distance from the oscillator source (cavity wall). The normalization factor of the ordinate was chosen so as to set the constant in Eq. (3) equal to 1. A far more accurate means of measurement is the *linewidth* (FWHM) of the resonance line shape,[11,12] since it involves only *relative* values of L. In terms of Fig. 3(a)

$$\text{FWHM}=\tfrac{1}{2}(\text{IP}_{max}+\text{IP}_{min}). \tag{12}$$

The relative cavity lengths L_1 and L_2 corresponding to FWHM are shown in Fig. 3(a). They can be found experimentally, and an *absolute* measurement of the FWHM$=L_2-L_1$ can be made. The measurement of the position of the FWHM on the ordinate must be made using the Zero-signal (IP=0 baseline) as the reference value, also shown in Fig. 3(a). Numerical calculations of the real part of Eq. (3), coresponding to the lock-in IP signal show that the linewidth changes with chopping frequency, f, and thermal diffusivity, α_g, as indicated in Figs. 4 and 5, respectively. The decreased linewidth (narrower resonance peak) with increasing frequency implies that the experimental sensitivity to gas thermal diffusivity changes, which induce peak shifts, improves at higher frequency cavity scans, provided the SNR remains satisfactory. This is consistent with the trends for increased cavity Q factor at overtone resonances, Table I. On the contrary, the increased linewidth with increasing thermal diffusivity predicts lower resolution for highly conducting gases (e.g., hydrogen or helium), which can be partly offset by increasing the frequency. The resonator can be easily cali-

brated owing to the essentially linear dependence of $FWHM^2$ with α_g. The correlation coefficient for a straight line of the type

$$\alpha_g = A \times FWHM^2 + B \tag{13}$$

is >0.9999 for the curves shown in Fig. 5. The effect of the cavity wall material enters the calculation through the coefficients γ_{jk}, Eq. (5).

The calibration of the cavity is most convenient with respect to air as the reference ambient gas. Based on the definition of b_{jk} in Eq. (5), these coefficients can explicitly carry a dependence on gas relative diffusivity with respect to ambient air by writing

$$b_{gp} = b_{ap}\sqrt{\alpha_g/\alpha_a}; \quad b_{gs} = b_{as}\sqrt{\alpha_g/\alpha_s}, \tag{14}$$

where the subscript "a" stands for "air." The advantage of Eqs. (14) is that, once α_g is known, all other diffusivities can be measured with respect to that value. The curves for cavities with Al, Cu, or brass walls have been calculated in Fig. 5 with thermophysical values taken from the data given in Sec. II B. It can be seen that thermophysically very different wall materials have little effect in the linearity or the slope of the curves in Fig. 5, which makes the thermal-wave resonator quite useful as a gas sensor. If the linewidth curve of Fig. 4 is plotted in the form $FWHM^2$ vs ω^{-1}, a straight line results, which may also be calibrated and used for gas diffusivity measurements.

Figure 6 shows experimental resonance lineshapes normalized by the PPE signal generated in the geometry of Fig. 1 by the direct incidence of the laser beam on the PVDF detector in the absence of the cavity. Both IP and Q channels are shown. Also shown is the theoretical fit of Eq. (3) to the data using an Al resonator wall 15 μm thick at $f=20$ Hz. The 20 Hz lineshape fit gave $\alpha_{air}=0.211\pm0.004$ cm^2/s for both IP and Q channels at ambient temperature of 21 °C. This value can be compared to the literature value of 0.22 cm^2/s (Ref. 13) quoted at 300 K. The value of the thermal diffusivity of air varies between 0.15 and 0.22 cm^2/s with ambient temperature change between 250 and 300 K.[14] Since the resonator experiments were performed under $T=294$ K conditions, the calculated value of the diffusivity using a linear dependence on ambient temperature is expected to be 0.21 cm^2/s. The present methodology has allowed the measurement of the thermal diffusivity of air to three significant figures with 1.9% accuracy and with numerical agreement from both lock-in channel signals.

ACKNOWLEDGMENT

We would like to acknowledge the support of Energy, Mines and Resources Canada for a contract to CHES which made this work possible.

[1] C. A. Bennett, Jr. and R. R. Patty, Appl. Opt. **21**, 49 (1982).
[2] L. D. Favro, P.-K. Kuo, and R. L. Thomas, in *Photoacoustic and Thermal Wave Phenomena in Semiconductors*, edited by A. Mandelis (North-Holland, New York, 1987), Chap. 4.
[3] A. Mandelis, J. Appl. Phys. **78**, 647 (1995).
[4] R. L. Thomas, J. J. Pouch, Y. H. Wong, L. D. Favro, P.-K. Kuo, and A. Rosencwaig, J. Appl. Phys. **51**, 1152 (1980).
[5] *Principles and Perspectives of Photothermal and Photoacoustic Phenomena*, edited by A. Mandelis (North-Holland, New York, 1991), and references therein.
[6] H. S. Carslaw and J. C. Jaeger, *Conduction of Heat in Solids*, 2nd ed. (Oxford, London, 1959).
[7] A. Mandelis, J. Vanniasinkam, S. Budhuddu, A. Othonos, and M. Kokta, Phys. Rev. B **48**, 6808 (1993).
[8] M. Munidasa and A. Mandelis, Rev. Sci. Instrum. **65**, 2344 (1994).
[9] H. Coufal and A. Mandelis, in Ref. 2, Chap. 7.
[10] Y. S. Touloukian, R. W. Powell, C. Y. Ho, and M. C. Nicolaou, *Thermal Diffusivity* (IFI/Plenum, New York, 1973).
[11] L. E. Kinsler and A. R. Fray, *Fundamentals of Acoustics*, 2nd ed. (Wiley, New York, 1962), Chap. 8.7.
[12] A. Yariv, *Quantum Electronics*, 3rd ed. (Wiley, New York, 1989), Chap. 7.3.
[13] *CRC Handbook of Chemistry and Physics*, 74th ed., edited by D. R. Lide (Chemical Rubber, Cleveland, OH, 1993), pp. 6-1 and 6-199 (air); p. 12-134 (Al).
[14] J. P. Holman, *Heat Transfer*, 7th ed. (McGraw-Hill, New York, 1990), p. 654.
[15] *Technical Manual, Kynar Piezo Film* (Pennwalt Corp., Valley Forge, PA, 1987), p. 15.